Anti-Counterfeiting Near-Field Chipless RIFD Tags Based on Laser-Induced Graphene on Cork

A. Lazaro, *Senior, IEEE*, M. Cujilema, R. Villarino, M. Lazaro, and D. Girbau *Senior, IEEE*

***Abstract*—This work presents non-cloneable RFID tags to protect products like wine, liquor, and oil from counterfeiting. The tags have a unique spectral response created by combining their shape and sheet resistance, using layers of conductive material. A laser-induced graphene (LIG) layer is formed on a cork substrate and then is electroplated to improve conductivity.**

Two prototype scanners that read the tags' electromagnetic signatures are presented, which are compatible with wine bottles and cork stoppers of different sizes. The first prototype relies on rotating the object during measurements, whereas the second uses four switched microstrip transmission lines as probes. Initial tests with complex logo images show the feasibility of this technology.

I. Introduction

THE wine industry faces significant challenges from counterfeit and adulterated products [1]. These fraudulent practices defraud consumers, undermine the reputation and economic stability of authentic wine producers, and pose potential health risks. To combat this, advanced technologies like holograms, QR codes, and RFID tags are employed. Additionally, blockchain technology is increasingly being used to track the supply chain and verify product authenticity. Companies also invest in secure packaging designs that are difficult to replicate.

Verifying the authenticity of an object involves more than just identification. Although conventional passive RFID has been suggested as an authentication solution [2], [3], most of these tags are susceptible to cloning [4] being only [5] the ones that support cryptographic authentication checks, which are much more expensive than regular crypto-less tags. Numerous anti-counterfeit technologies are documented in the literature, since RFID tags can be easily stolen, lost or cloned by attackers. For instance, concerning chip-based RFID, strategies to make tags unclonable have been proposed, such as including the development of physical unclonable functions (PUFs) using fingerprints [6], [7] or embedding software/hardware security features [4], [8]. On the other hand, there are also several studies proposing various solutions to increase security in chipless RFID tags and make their cloning more difficult [9]–[12]. Most of these solutions are based on designing tags with a specific radio frequency fingerprint and a high level of randomness. The works [13], [14] implement tags from barcodes printed with ink or engraved on conductive sheets. In [15], the fingerprints are based on the nano-structured composite materials. In [9], security authentication is performed by dipoles engraved on a rigid substrate, having a size like that of a credit card. In [16], the authors propose two chip-free solutions operating in two different frequency bands (RF and THz), demonstrating that in both bands the geometric tolerances derived from their manufacturing produced drifts in the spectral responses. In work [17], tags are developed to be embedded into the final product. These tags are based on printing multiple coupled C-shaped characters. Another type of printed tag is the one presented in [18]. A conventional C-fold printed tag is proposed, optimized by introducing discrete square box patterns along the arms of the C-fold disperser to increase its sensitivity to inkjet printing. In [10], the use of a chipless RFID tag based on concentric slot annular resonators with dimensions like those of a QR code is proposed, whose frequency response generates a unique identifier, since it depends both on the geometry of the slot and is sensitive to manufacturing tolerances and on the electrical properties of the substrate. In [19], [20], several tags that act as an RF fingerprint, thanks to the insertion of random wires inside a dielectric sealant are presented. A similar procedure is used in [21], which is based on the additive manufacturing technique. Chipless tags based on near-field readable resonators have also been proposed [22]. Finally, other works [23]–[25] use ML and DL (Machine and Deep Learning) techniques to facilitate the detection of the electromagnetic signatures of the tags and thus retrieve the information.

Recently, laser-induced graphene (LIG) has garnered significant attention for its application in sensing and in energy storage devices, such as supercapacitors and batteries [26]. LIG is utilized to develop high-sensitive gas sensors [27], biosensors for medical diagnostics, and flexible strain sensors for wearable devices [28], [29]. While most research uses polyimide [30], [31] as a precursor, other eco-friendly substrates like wood [32] and cork [33], [34] can also be employed.

In addition to the applications mentioned above, graphene has been recently explored in some radiofrequency applications. Graphene coils for RFID applications manufactured using spray printing techniques on a flexible substrate such as textile have been presented in [35]. UHF RFID tags made with LIG antennas have been proposed in [36], [37]. A flexible UHF RFID sensor for triethylamine based on an interdigital capacitor has been presented in [38], where the tag was also manufactured with LIG using polyimide (Kapton) as a precursor. Finally, the losses due to the LIG allow to improve

Manuscript received March xx, 2025; accepted April xx, 2025. Date of publication May xx, 2025. This work was supported by the Spanish Government grant PID2021-122399OB-I00 and the grant PRE2022-103744, funded by MCIN/AEI/10.13039/501100011033 and by the EU's European Regional Development Fund (ERDF).

The authors are with the Electronics, Electrical and Automatics Engineering Department, Rovira and Virgili University, Tarragona, Spain (e-mail: antonioramon.lazaro@urv.cat, marco.cujilema@urv.cat, ramon.villarino@urv.cat, marc.lazaro@urv.cat, david.girbau@urv.cat). The corresponding author is A. Lazaro (e-mail: antonioramon.lazaro@urv.cat).

the absorption of frequency selective surfaces (FSS) fabricated on polyimide [39], [40] or wood [41].

In a previous work [34], the authors presented a method to fabricate chipless tags engraved on cork stoppers for authentication purposes. These tags have unique electromagnetic signatures associated with multiple frequency resonances and attenuations that can be measured by the reader. The strips and images that form the tags are engraved directly on the cork using LIG techniques, instead of using conductive inks. However, since the conductivity of LIG is relatively low compared to that of the conductors typically used in radiofrequency applications, it is necessary to apply a nickel electroplating process on the LIG traces to improve the quality factor of the resonances, which also adds an additional degree of randomness thanks to the different parameters selected in the manufacturing process. Regarding the reader, an important novelty of this work is the replacement of the mechanical scanning system used in previous works [31] [34] by a static system consisting in the sequential measurement of the tag based on electronic switching. By measuring the transmission coefficient of four microstrip probe lines located over the tag, controlled by a microwave switch, and using a vector network analyser (VNA), this work demonstrates that the measurement throughput is increased, simplified, and shortened, making the use of cumbersome mechanical readout systems unnecessary. This improvement is shown in this paper by comparison to results obtained with previous mechanical systems. In addition, this study introduces criteria for the statistical classification of tags based on the comparison of specific metrics with reference data stored in a database. Tags that are not present in the database are classified as counterfeit. To support this classification, a threshold level is determined using boxplots generated from previously stored tag measurements. This threshold can be dynamically updated each time a new tag is added to the database. In addition to the root mean square error (RMSE) between tags, alternative metrics such as the correlation coefficient have also been explored in this work. Extending beyond the previous work, this study further investigates sources of error related to tag position and environmental influences, such as variations in cork permittivity due to moisture absorption.

The remainder of the document is organized as follows: Section II details the tag manufacturing process and the proposed reader. Section III presents the experimental results. Finally, Section IV offers some concluding remarks.

II. Proposed System

The authentication system consists of three steps described below and summarized in the block diagram in Fig. 1.

The first step is the manufacturing of the tag, which consists of resonators engraved as a LIG image, printed directly with a CO_2 laser. The layout dimensions, shape, and materials determine the resonance frequencies and electromagnetic response. The laser parameters used in the manufacturing process influence the conductivity and thickness of LIG layer. While the resulting conductivity is relatively high and suitable for many sensor applications, it is insufficient for resonators requiring high-quality factors. The resonator is subjected to electroplating processes for different time intervals to improve its conductivity and achieve an additional degree of uncertainty, depending on the thickness of the deposited metal layer [31].

In the second step, the electromagnetic signature of the tag is determined. It is characterized using a custom-designed near-field reader compatible with wine bottles. Data are stored in a database that will later be used to compare it with the tag to be authenticated.

Finally, the last step is the checking of the tag by measuring its EM signature and comparing it with the one stored in the database in step 2. To this end, the root mean square error (RMS) is used as a metric for the comparison between the signature stored in the database and the measured signature of the tag that has to be validated.

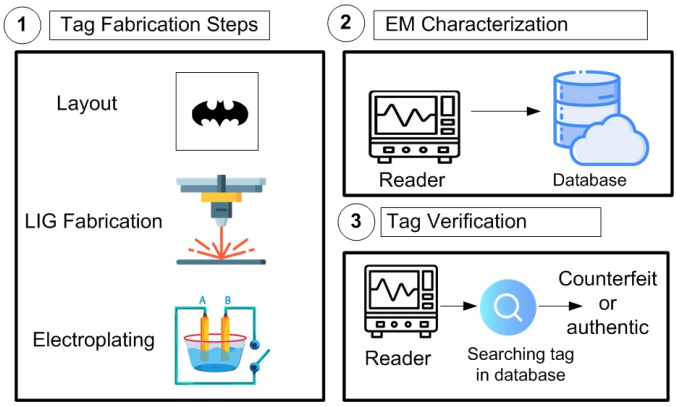

Fig. 1. Diagram of the proposed authentication system that includes the manufacturing of the tag, its EM characterization, storage in the database, and the verification step.

Tags manufactured with identical designs and parameters are expected to show similar responses, with RMS errors being lower than those obtained with different tags. Measurement repeatability errors lead to variability in the RMS error. As a result, the probability distribution of the RMS error can be defined either considering a single tag (intra-tag) or several tags (inter-tag) [17]. The intra-tag probability density function represents the probability distribution of RMS errors between measurements performed with the same tag class. On the contrary, in the inter-tag probability density function, these measurements are made between different types of tags. These probability distributions are schematically shown in Fig. 2. The assumption of a specific tag in the database - which will allow its post identification - is determined when the measured RMS error falls below a certain threshold. The selection of this threshold directly affects the probability of error.

Excluding systematic errors, which should be treated as outliers and are mainly attributed to inconsistencies in the position of the tags inside the scanner, the main source of error is measurement noise. This noise is associated with calibration errors in the VNA and with the aging of the calibration itself. Such errors, typically less than 0.05 dB [42], which generally increase at higher frequencies, can be estimated by comparing the measured S-parameters with calibration standards. The calibration error associated with

the VNA used in these measurements is typically less than 0.008 dB. Maintaining a stable temperature and performing periodic VNA calibrations (e.g. every hour) can help reduce or maintain this error at a nearly constant level. Once the metric (RMS error in our case) is defined, the probability density of the RMS error between a measurement and recorded data for each tag pair can be evaluated. Since random errors arise from a combination of several independent sources or factors and frequencies, the central limit theorem suggests their distribution can be approximated by a Gaussian probability function [43], [44]. As the tags are distinct, the underlying random processes are assumed to be independent. In that case, only the mean and standard deviation are required to describe the Gaussian probability function:

$$f_{ij}(RMS_{ij}) = \frac{1}{\sigma_{ij}\sqrt{2\pi}} e^{-\frac{(RMS_{ij}-\mu_{ij})^2}{2\sigma_{ij}^2}} \quad (1)$$

where RMS_{ij}, μ_{ij}, and σ_{ij} are the RMS error, the mean RMS error, and the standard deviation between tag i and tag j, respectively.

By measuring tags multiple times, the standard deviation is typically estimated to be 0.02 dB for intra-tag measurements and 0.025 dB for inter-tag measurements. These values are on the same order of magnitude as the calibration errors, considering the increase due to calibration aging and repeatability errors arising from minor residual angle misalignments. Manufacturing repeatability also contributes to variability. If each tag is considered unique, only random noise should be considered. Tags manufactured with similar parameters are expected to exhibit similar responses. Therefore, if grouped within the same class, intra-tag errors primarily reflect manufacturing repeatability and tolerances of the parameters that characterize the material. Maximizing the difference between the mean intra-tag and inter-tag RMS values is therefore important to ensure the system's robustness to systematic error (e.g. positioning errors).

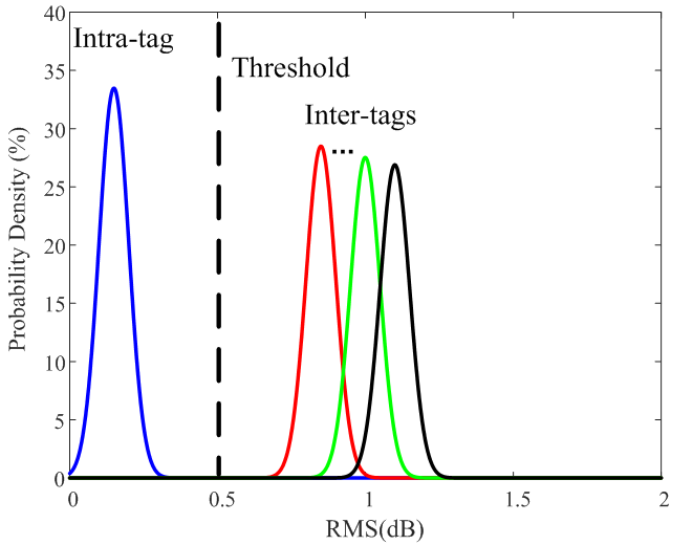

Fig. 2. Probability density function of the RMS error (in dB) for intra-tags and inter-tags, including the threshold.

A. Tag Manufacturing

The tag manufacturing process has been described in detail in [34] and is summarized in this section. A CO_2 laser engraver and cutter (FLUX Beambox 40W, Kontich, Belgium) with a wavelength of 10.6 μm and a maximum power of 40 W is used for the LIG fabrication. The resolution of the laser is 1000 dpi and its beamwidth is 50 μm. The average power radiated over the cork is controlled by adjusting the duty cycle with pulse width modulation (PWM). The LIG on the cork is generated when the laser reaches a specific irradiation energy threshold, initiating the formation of the conductive graphene-derived material [33]. The conductivity and morphology of LIG depend on the laser parameters, such as the duty cycle (or equivalently, the average laser power) and the scan speed [45].In this work, the laser beam is scanned on the cork substrate at a speed of 20-24 mm/s with a duty cycle of 10-14%. The combustion of the cork occurs at average power levels that exceed these values.

Various types of cork stoppers exist, each tailored to specific types of wine and their respective aging processes [46]. Thus, the feasibility of using commercial cork as a precursor for graphene has been investigated. Commercial stoppers from AR Estrategias (Badajoz, Spain) were used in the study. Cylindrical stoppers made of natural cork, composed of cork powder and water-based glue of different grain sizes, have been analysed. Type A and D corks are those with the smallest and largest grain size, respectively (see photographs included in Fig. 3). Raman spectroscopy is a widely used method for characterizing LIG material [47].

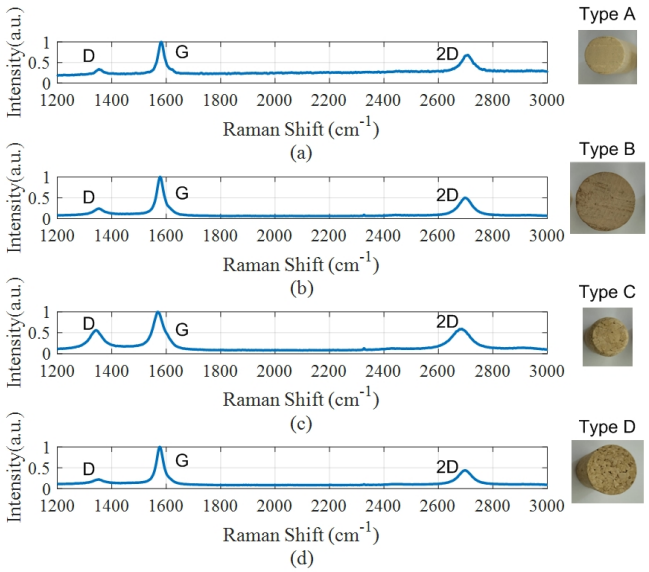

Fig. 3. Normalized Raman spectrum for various types of cork stoppers, all with similar sheet resistance. Stoppers are manufactured using a laser with a 12% duty cycle, a speed of 24 mm/s, and a maximum power of 40 W. Characteristic peaks are observed at frequencies D, G, and 2D for each type: (a) Cork A (R_s=13.8 Ω/sq), (b) Cork B (R_s=14.8 Ω/sq), (c) Cork C (R_s=17.6 Ω/sq), and (d) Cork D (R_s=14.0 Ω/sq). A photo of each cork stopper is displayed on the right for each case.

Test structures consisting of a 1 cm long and 2 mm wide

strips were manufactured. Figure 3 shows the Raman spectrum measurements corresponding to different LIG samples performed under the same conditions (duty cycle (12%) and speed (24 mm/s)) for different kinds of cork stoppers [34]. They were obtained using Renishaw's InVia confocal Raman microscope. The Raman spectrum of graphene is characterized by three peak frequencies (denoted as G, D, and 2D bands), each of which provides information about its structure and properties. The G peak at 1592 cm^{-1} denotes the primary vibrational mode of graphene. The D peak at 1350 cm^{-1} is commonly used to assess the level of disorder or defects in the graphene structure. The 2D peak at 2685 cm^{-1} is sensitive to the number of graphene layers and provides insights into the electronic structure. A high 2D peak value in LIG indicates the presence of well-ordered, multilayer graphene structures, which are advantageous for applications requiring high electrical conductivity and mechanical strength. The obtained 2D/G ratio values are in the range of 0.4 to 0.6, while in all samples D/G ratios less than 0.5 are observed, indicating a low presence of defects.

The sheet resistance of the samples was measured with a multimeter (Keysight Tech., model 34450A) using a special probe designed with a flexible copper ribbon to avoid damaging the LIG surface. The resistance of the wires was subtracted to eliminate both the probe and the interconnection wire contributions. Samples showing a higher ratio between the 2D and G peaks indicate higher sheet resistances. To investigate the optimal laser duty cycle, or equivalently, the average laser power, the average sheet resistance, and its standard deviation are measured as a function of the duty cycle. The results are summarized in Table I. Sheet resistance decreases approximately linearly as a function of the duty cycle. Observations indicate that for duty cycles above 12% (corresponding to an average power of 4.86 W), the cork surface begins to burn. Cork samples C and D, with larger grain sizes, show greater variability between samples, attributed to their granulometry. Therefore, the parameters chosen for tag manufacturing were a duty cycle of 12% and a processing speed of 24 mm/s.

Duty cycle	Type A	Type B	Type C	Type D
10%	24 ± 1.0	25.8 ± 1.9	33 ± 2.9	43.5 ± 4.3
12%	17.7 ± 1.4	14.8± 1.0	17.6 ± 1.1	14.0 ± 0.8
14%	13.9 ± 1.2	4.5 ± 0.4	6.1 ± 0.6	8.9 ± 1.0

TABLE I
MEASURED SHEET RESISTANCE AND DEVIATION IN Ω/sq AS A FUNCTION OF THE LASER DUTY CYCLE AND CORK TYPE.

To reduce the sheet resistance and improve the quality factor of the resonances, specially in the higher frequency bands, the LIG traces are nickel-plated. Although other metals can be used, nickel electroplating provides good adhesion and corrosion protection [48]. This additional step introduces more variability into the manufacturing process, which increases the complexity to clone the tag.

During the electroplating process, parts previously patterned with LIG are connected to the cathode, while a nickel rod serves as the anode. A nickel-plating solution from MARAWE GmbH & Co. KG (Regensburg, Germany) consisting of nickel sulphate, is used as the electrolyte. A DC power source (Agilent E3632A model), configured as a current source, supplies a constant current. During the electroplating process, the current flowing through the solution is typically set between 20 mA and 40 mA.

Since the conductivity of laser-induced porous graphene is relatively low (reported values range from 200 to 2500 S/m [47]), the effective conductivity of the embedded resonators is mainly due to the high conductivity of nickel ($1.43 \cdot 10^7$ S/m). Nickel begins to penetrate the porous structure of the graphene, gradually covering the entire surface. As the nickel layer covers the surface, its thickness increases, leading to a faster decrease of the sheet resistance. The infiltration and growth of the nickel layer can be observed in a vertical cross-section, as shown in the Scanning Electron Microscopy (SEM) image in Fig. 4.a. Energy-dispersive X-ray spectroscopy (EDS) analysis is used to determine the layer composition. Fig. 4.b shows the presence of carbon (red) and clearly reveals how nickel (blue) gradually infiltrates through the porous structure of the LIG.

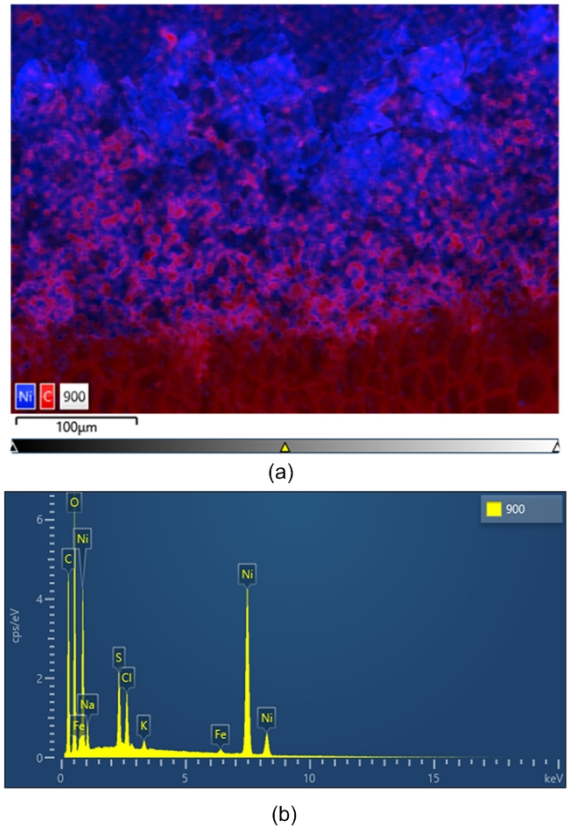

Fig. 4. SEM images of type A cork fabricated with the following parameters: duty cycle of 12% and 24 mm/s, electroplating time of 900 s with a current of 23 mA: (a) cross-section of the interface corresponding to the ordered multilayer structure of graphene and nickel layer showing the composition (blue Nickel and red Carbon), (b) EDS Spectrogram

The effective conductivity is obtained from the weighted average of the conductivities of LIG and nickel, weighted in turn by their respective thicknesses (see Fig. 5). The effective conductivity of the LIG and nickel layers as a function of the electroplated thickness t_p is modeled using the following expression [34]:

$$\sigma(t_p) = \begin{cases} \frac{\sigma_{LIG} t_{LIG} + \sigma_1 \cdot t_p}{t_{LIG} + t_p} & , t_p \leq t_{th} \\ \frac{\sigma(t_{LIG})(t_{LIG} + t_{th}) + \sigma_2 \cdot (t_p - t_{th})}{t_{LIG} + t_p} & , t_p > t_{th} \end{cases} \quad (2)$$

where t_{LIG} is the thickness of the LIG, which is 500 μm (extracted from SEM images); t_{th} is the threshold thickness for modeling the roughness and porosity of the LIG surface. This parameter is determined from the instant where the slope in the sheet resistance changes and a value of 1.2 μm was obtained. A value of the conductivity of the LIG (σ_{LIG}) of 2500 S/m was considered from the measured DC sheet resistance. The conductivities of the electroplated metal inside (σ_1) and on (σ_2) the LIG are treated as fitting parameters. The fitted values were $\sigma_1 = 5.5 \cdot 10^6$ S/m and $\sigma_2 = 1.02 \cdot 10^7$ S/m, respectively. These values are lower than the bulk nickel conductivity, likely due to the porosity and roughness of the electroplated surface. The thickness t_p is obtained from the electroplating time determined by Faradays's law [31], [34], [49]. This thickness is proportional to the product of the electroplating time and the electrical current that flows through the solution.

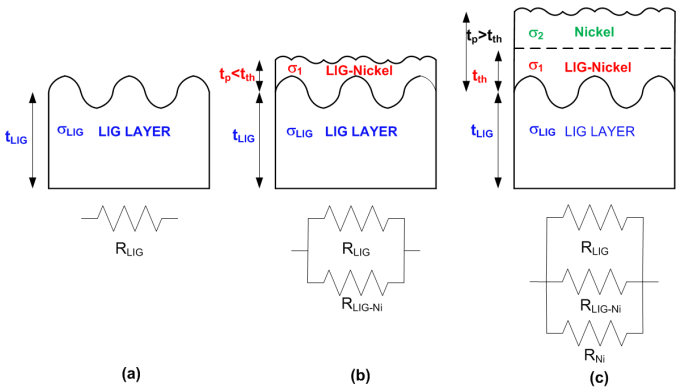

Fig. 5. Cross section schema used to compute the effective conductivity from the parallel resistance of the different material layers. (a) Only LIG layer, (b) for electroplating thickness $t_p < t_{th}$ and (c) for electroplating thickness $t_p > t_{th}$.

Fig. 6 shows the measured decrease of the sheet resistance as a function of the electroplating time. Once the desired thickness of the metal coating is reached, the cork stopper is removed from the electrolyte bath, rinsed, and dried. Good agreement has been obtained between the measured sheet resistance and that modeled using the conductivity model. Therefore, by controlling the electroplating time, it is possible to manage the sheet resistance and, consequently, the quality factor of the resonators (see [31]). In addition, the dependence on electroplating time introduces a degree of randomness, increasing the variability of the tags and making cloning difficult if this parameter is unknown.

B. Scanner Design

The system is based on coupling a microstrip line, which serves as a near-field probe of the tag When the conductive traces of the tag are near the line, absorptions in the line transmission coefficient occur at the resonance frequencies of the tag. This coupling is due to both magnetic coupling,

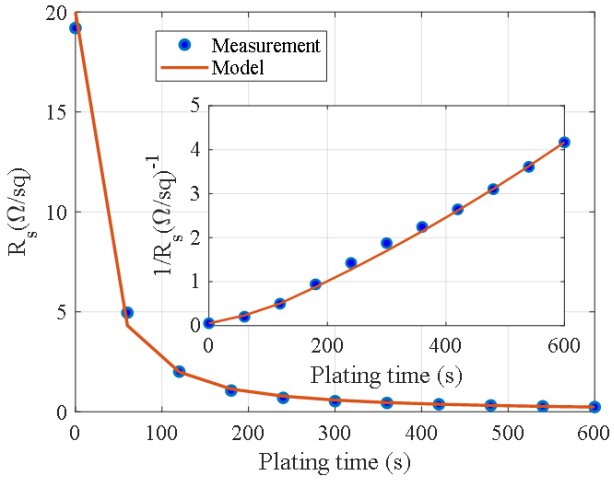

Fig. 6. Comparison between measured and modelled sheet resistance as a function of electroplating time at 23 mA. The inset shows the inverse of sheet resistance.

which arises from mutual inductance, and due to capacitive coupling, resulting from the capacitance between traces. Depending on the orientation and distance of the tag relative to the line, certain resonance frequencies may not be detected. The absorption level and bandwidth are influenced by the distance, relative position of the line to the traces, the quality factor and material loss. Figure 7 schematically illustrates an example. Figure 8 shows a typical coupling mechanism between a microstrip line and well-known resonators, as well as their equivalent circuits around the resonance frequency [50]. To excite different resonance frequencies, the relative position of the line is changed, and since these frequencies are not known, a broadband probe is required. In consequence, two methods can be considered: mechanical scanning and electronic scanning.

C. Mechanical scanner

The first scanning method involves moving the tag on the line means of a linear actuator, and it was proposed in a previous work [31]. Another possibility, more appropriate for the application proposed in this paper, is to rotate the engraved tag onto the bottle cap [34]. Figure 9 shows a photograph of the setup developed with the mechanical rotating scanner. A vector network analyzer (Agilent PNA E8364C) measures the transmission coefficient (S_{21}) between the two ends of the microstrip through line used as probe (with two SMA launch connectors at its ends). The microstrip line characteristic impedance is 50 Ω manufactured on a 20-mil thickness substrate (Rogers RO4003C). The tag under test is rotated by means of a stepper motor that includes a gearbox connected to a rotary table, allowing the VNA to scan the electromagnetic response while rotating. An isolation 75 μm Kapton sheet is used as a spacer between the probe line and the tag to ensure a constant gap.

Experiments are conducted by rotating the tag in 10-degree steps, acquiring 1601 points in the frequency range from 100 MHz to 12 GHz for each angle. Since only the magnitude

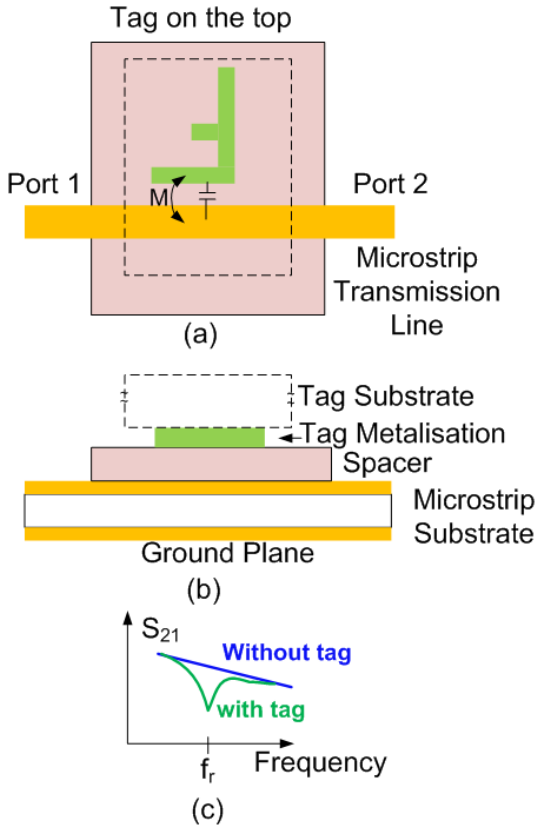

Fig. 7. Schematic showing a tag of arbitrary shape printed on a substrate and coupled to a microstrip transmission line: (a) top view, (b) Cross-section, (c) Response of the transmission coefficient of the line in presence or absence of the coupled tag. A thin dielectric (Kapton) spacer is inserted between the microstrip line and the tag when the tag is printed on cork without protection, to prevent short-circuits.

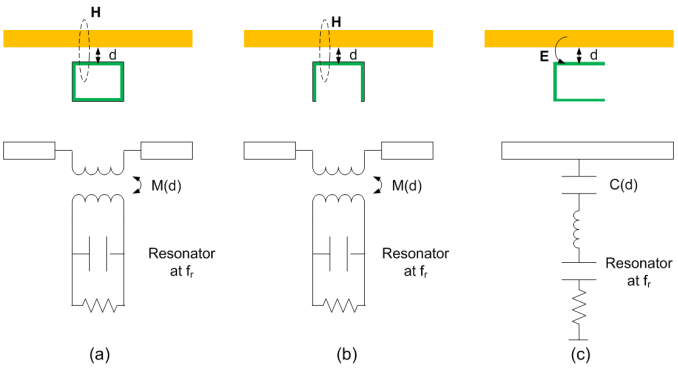

Fig. 8. Examples of different resonators coupled to a microstrip line and their equivalent circuits: (a) ring resonator magnetically coupled to a line, (b) C-shaped resonator magnetically coupled to a line, and (c) C-shaped resonator electrically coupled to a line.

of S_{21} is needed, a scalar system (e.g., spectrum analyser including a tracking generator) could also be used to reduce costs. The S_{21} frequency response drops when the transmission line passes a position coupled to a resonance. Extending the measured frequency range also reveals the presence of multiple harmonics associated with these resonances.

The measured S_{21} parameter for each tag is stored in a database to allow the future verification, which consists of measuring the tag again using the same settings, and comparing the new response to the one stored. In case of mismatch, the tag is considered counterfeit.

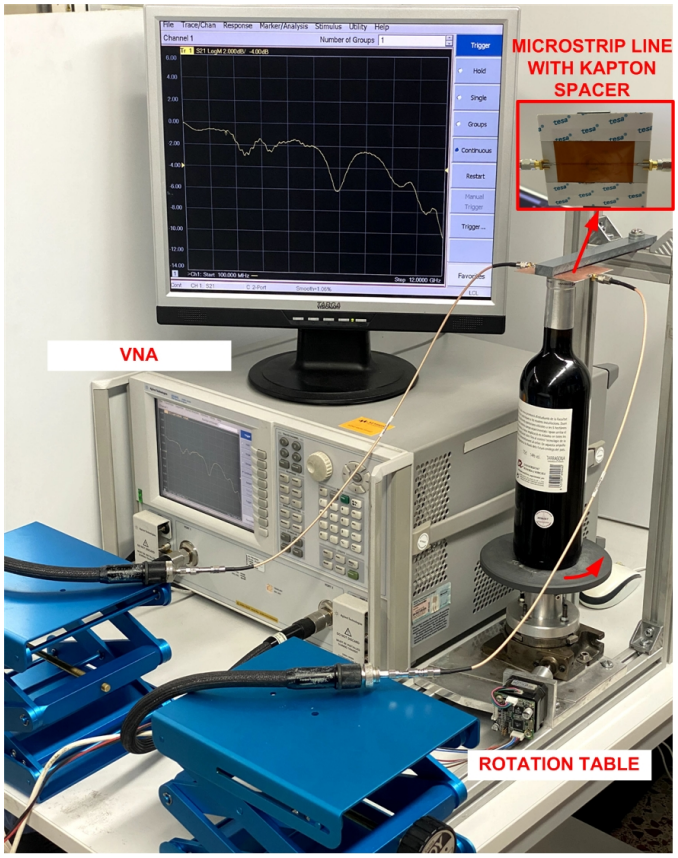

Fig. 9. Photography of the experimental setup based on a mechanical rotating scanner.

D. Electronic scanner

As an alternative to this mechanical approach proposed in a previous work [34], which normally is embarrassing, a novel method based on sequentially measuring the tag is proposed. It is based on measuring with a VNA the transmission coefficient of four microstrip probe lines located on top of the tag, using microwave switches to select the line that is measured. By reducing the number of measurements to just four, using electronic switching and avoiding mechanical rotation, measurement performance is increased. A proof of concept setup developed to evaluate its performance is shown in Fig. 10. The lines have been designed to be sufficiently spaced to ensure they are decoupling and can excite resonators in orthogonal orientations. The input and output of each line

are connected to the VNA ports with two single-pole four-throw (SP4T) switches. In this prototype, the commercially available electromechanical SP4T RMM-SR001 (RelComm, USA) switches are used. MMIC-based broadband switches can be integrated into future prototypes to reduce loss associated with interconnections, as well as reduce switching time. Similar to the mechanically rotating prototype, the microstrip transmission lines' characteristic impedance is 50 Ω and are fabricated using a 20 mil thick substrate (Rogers RO4003C). Additionally, a 3D-printed support has been designed to align the tag to test various types of stoppers.

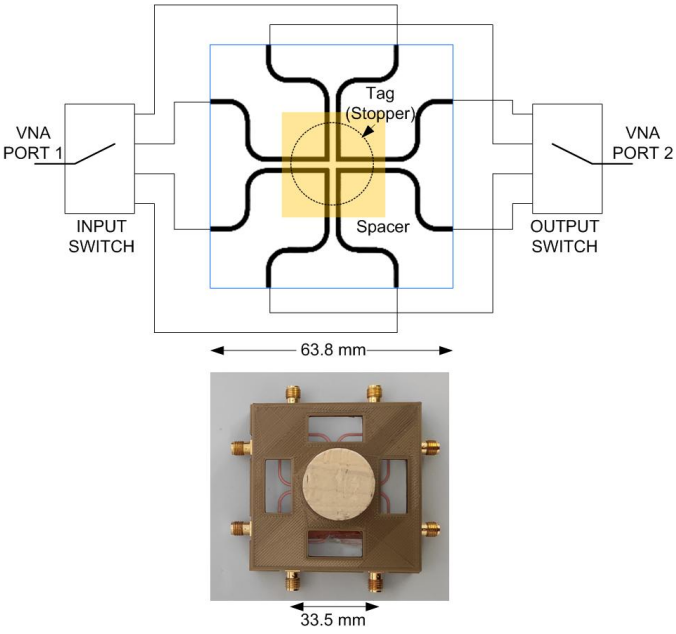

Fig. 10. Diagram of the switched scanner (top) and photograph of a cork stopper aligned to the scanner (bottom).

Figure 11 shows a simulation example made with Keysight PathWave Momentum. The "F" logo with dimensions 10 mm × 7 mm is centered over the four microstrip lines, as shown in Fig. 11. A 75 μm Kapton sheet is again used as spacer between the lines and the stopper. A 2-cm thick layer of cork is added to simulate the bottle stopper, with a relative permittivity of 1.5 and a loss tangent of 0.03 [51]. Simulations are performed with and without (background) the logo. In addition, the sheet resistance of the conductor logo is varied to examine its influence on the results. Sheet resistances of 5 Ω/sq, 1 Ω/sq, 0.5 Ω/sq and 0.25 Ω/sq, corresponding to electroplating times of 50 s, 150 s, 300 s, and 600 s, are considered. The case of using copper(Cu) conductor is also simulated as a reference (thickness 17 μm, conductivity $4.7 \cdot 10^7$ S/m). Fig. 12 shows the transmission coefficients for each line. It is observed that the presence of conductive materials on some of the lines significantly increases the transmission loss. In the cases of lines 2, 3 and 4, resonances were excited. The resonance frequency depends on the size and shape of the conductive traces. The quality factor of these resonances decreases rapidly as the sheet resistance increases, which depends on the electroplating time. Line 3, on the other hand, was hardly affected, except for an increase in losses associated with the cork, since the metallic parts were far away from this line. Line 3, being far from any strip, exhibits the transmission coefficient of a simple transmission line without resonance. In contrast, Lines 1 and 4 excite a single resonance, associated with the open-ended stub at the lower edge of the character. The coupling in Line 4 is stronger than that in Line 1, resulting in a deeper notch. Line 2 excites two resonances linked to the edges of the character "F." Due to the similar lengths of these edges, the corresponding resonances are very close and therefore overlap. However, for complex images, identifying the origins of the resonance becomes more difficult, and predicting the EM signature is more challenging. These simulations demonstrate the ability of the proposed scanner to detect electromagnetic signatures without the need to rotate the sample.

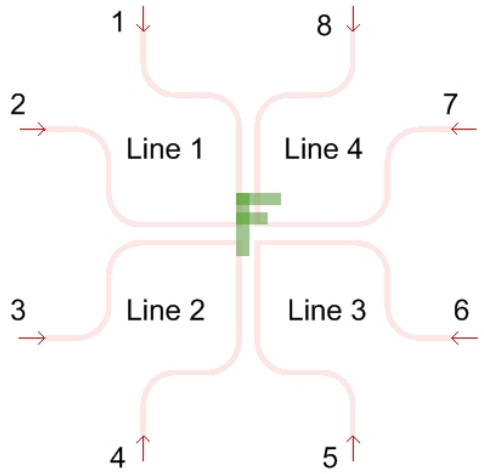

Fig. 11. Layout of the simulated probe lines and "F" character.

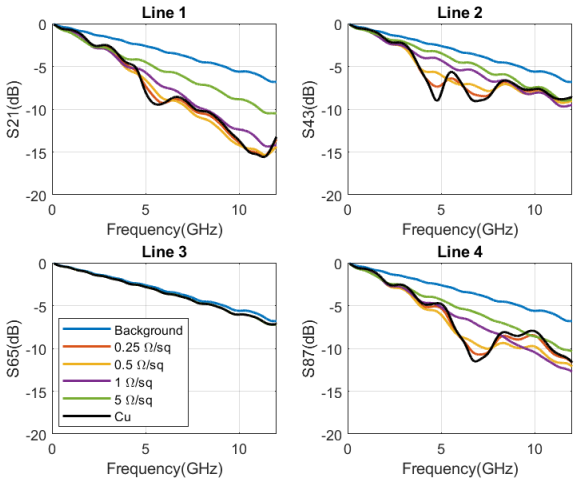

Fig. 12. Simulated S parameters for each line without the tag (background) and with the tag using different sheet resistances and copper conductor (Cu).

III. Experimental Results and Discussion

An example of the measurement of different tags using the mechanical rotating scanner is shown in Fig. 13. The tags, engraved on cork stoppers, feature three designs composed of the letters A, F, R, plus the New York Yankees logo, to consider a more complex design. The engraving is performed with a duty cycle of 12% and a speed of 24 mm/s. To calibrate the loss of the four lines, the measurement of the parameter S_{21} without tag is used as a reference (background). This background measurement is subtracted from the measurement obtained with the tags, thereby correcting microstrip probe line losses and enhancing the resonances. A method based on calculating the root mean square (RMS) error of the corrected S_{21} (in dB) is applied to classify the tags. The RMS between two tags, i and j, can be computed using the following expression:

$$RMS(i,j) = \sqrt{\frac{1}{N_a \cdot N} \sum_{k=1}^{k=N_a} \sum_{n=1}^{n=N} |dB(|S_{21i}(k,n)|) - dB(|S_{21j}(k,n)|)|^2} \tag{3}$$

where N and N_a are the number of measured frequencies and angular positions, respectively.

Table II presents the computed error between pairs of tags from Figure 13. The average of five measurements is shown. A tag is identified if the RMS error is less than a threshold set at $3 \cdot 10^{-2}$ dB (three times the difference between the same tag), taking into account the uncertainty in the VNA measurement. Table II demonstrates that tags can be perfectly distinguished from each other.

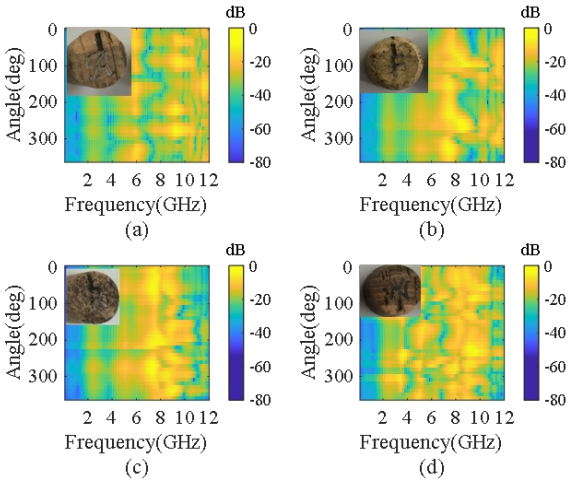

Fig. 13. Corrected S_{21} measurements with the mechanical rotating scanner of four different tags as a function of the frequency and angular position: (a) Character A, (b) Character F, (c) Character R and (d) Logo NY.

Experimental results performed with the electronically switched scanner are shown in Fig. 14. This figure shows the corrected frequency response (subtracting the measurement made without the tag) for each line. It is observed that in certain lines some resonances are detected, while on others, either because they are further apart or because they have a very weak coupling, resonances are barely perceptible. Specifically, two tags with the same shape (character F) but with different electroplating times (100 s and 900 s) have been measured. The metallization time was 900 s in the remaining cases and the currents were 24 mA in all of them. It was observed that resonance levels were weaker when using tags with conductors having higher surface resistances, due to the degradation of the quality factor and increased losses. As a result, resonances at higher frequencies were not detected in these tags. This introduces a degree of randomness if the parameters used to create the tags are unknown. An adhesive layer (e.g. PVA) or paint can be added over the LIG metallization to conceal the printed image. If this tag were to adhere to the protective plastic of the bottle, the shape would be invisible, and if one tried to remove it, the metallization would be partially destroyed, adding an additional security mechanism that would make cloning the tags more difficult. In these experimental measurements, a thin sheet of Kapton has been used to simulate the wrapping. This dielectric layer only causes a slight frequency shift in the resonances which is not a drawback for this application. Table III compares the RMS error, of the four lines, between the tags shown in Fig. 14 demonstrating that they are distinguishable despite only four lines are used. The RMS is computed with (3) but in in this case N_a is the number of probe lines used in the measurement. In these measurements, simple shapes such as characters have been used as tags, but arbitrary complex images could also be utilized.

TABLE II
Root mean square (RMS) error of the measured S_{21} between tags shown in Fig. 13.

Tag	a	b	c	d
a	0.01	1.18	1.76	1.76
b	1.18	0.01	1.63	1.78
c	1.76	1.63	0.01	1.75
d	1.76	1.78	1.75	0.01

TABLE III
Root mean square (RMS) error of the measured S_{21} between tags shown in Fig. 14.

Tag	a	b	c	d
a	0.01	0.96	1.18	0.63
b	0.96	0.01	1.05	0.75
c	1.18	1.05	0.01	0.87
d	0.62	0.75	0.87	0.01

To determine the optimal threshold, Fig. 15 presents a boxplot obtained with MATLAB from a dataset of 10 measurements taken on 20 different tags measured with the electronically switched scanner. This graph shows the minimum and maximum RSM error values. The bottom edge of the rectangle indicates the first quartile (Q1), which is the value below which 25% of the data fall. The center line represents the median (or second quartile), and the top edge of the rectangle provides information about the third quartile (Q3), or the value below which 75% of the data falls. Two different classes

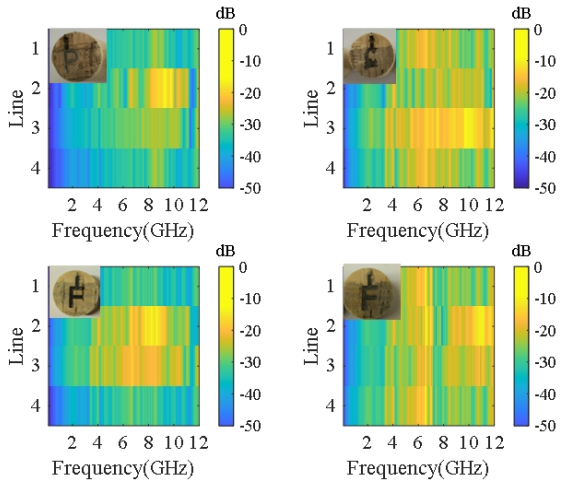

Fig. 14. Corrected S_{21} measurements with the electronically switched scanner of four different tags as a function of the frequency and angular position: (a) Character P, (b) Character C, (c) Character F (100 s electroplating time), and (d) Character F (900 s electroplating time). The electroplating time is 900 s except for case (c) that is made with 100 s of electroplating time.

are analyzed: intra-tag and inter-tag. The intra-tag variability considers the repeatability of the switches, the degradation of calibrations over time, and minor alignment errors of the tags in the scanner. In contrast, the inter-tag variability is primarily due to differences in the electromagnetic signatures of the tags, which are more significant than the intra-tag variability, resulting in greater deviations. The results show that the distributions of these classes do not overlap and therefore, a threshold can be selected at approximately the midpoint (around 0.3). In this dataset, the minimum level of the boxplot is associated with tags that have an identical layout but manufactured with different electroplating times. As new tags are added, the threshold can be updated, because the box plot is dynamically recalculated.

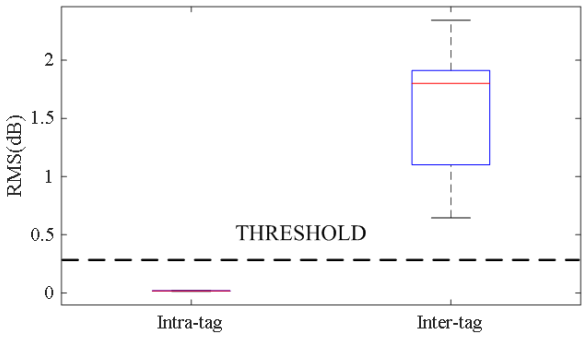

Fig. 15. Threshold determination based on the boxplot of the intra-tag and inter-tag measured RMS error.

While the root mean square error is a reasonable magnitude for quantifying the similarity between electromagnetic signatures, another distance-based metric could be used. The authors have investigated the use of the correlation coefficient between the measured data stored in the dataset. This metric has been previously used in chipless applications [17] but referred to far-field measurements. In that case, the correlation coefficient was used to reduce the influence of multipath interference, which is not present in near-field systems such as the one proposed in this work. Fig. 16 shows the box plot of the Pearson correlation coefficient. The correlation coefficient between the same tags (intra-tag) is practically 1. However, the inter-tag correlation coefficient is significantly lower, and a threshold can be selected to separate both classes. Since measurements are essentially different when resonances occur, several frequency points contain similar values; therefore, this set of points is correlated with other tags, resulting in relatively high correlation coefficients. The correlation coefficient tends to compensate for amplitude variations, which are important in this application, because changes in manufacturing parameters produce changes in the conductivity and in the quality factor, and consequently in the depth of the resonances. Another candidate to use as a similarity metric could be the joint entropy of the spectrum [52]. The normalized power in each frequency bin is treated as a probability distribution, and the Shannon entropy of that distribution is then calculated. In information theory, joint entropy measures the uncertainty associated with two or more random variables taken together, and it is used to measure the mutual information between signals. However, applying this metric to distinguish intra-tag from inter-tag characteristics proved unsuccessful. High entropy values were obtained, but the difference between tags was not sufficient. One possible reason that prevents a clear classification is that certain parts of the spectrum, specifically those corresponding to unexcited resonances, have similar values in different tags. In addition to previous metrics, other proposed algorithms to improve notch detection in chipless RFID such as the dynamic time warping (DTW) for spectral alignment proposed in [53] could be investigated in future works.

Figure 17 presents the RMS error of five tags fabricated with the same parameters, relative to a designated reference tag. A ”F” character was printed in the tags which were made using a 12% duty cycle, a 24 mm/s scanning speed, and a 900 s electroplating time at 23 mA. The observed repeatability of the switched system is below 0.04 dB. This error, which arises from manufacturing tolerances, measurement uncertainty of the network analyser and residual misalignments, is notably smaller than the approximate threshold of 0.3. Based on these results, it can be concluded that tags manufactured using the same cork type (to reduce the randomness due to the presence of granules), with the same layout, and identical manufacturing parameters cannot be distinguished by the system. However, without prior knowledge of these specific parameters, it is not possible to accurately replicate or clone the tag. This opens the possibility of using identical tags to protect a series of products. To further improve security, variations in the manufacturing parameters can be introduced. However, these variations result in tags that the system treats as different, and therefore, their data must be stored and managed within the database accordingly.

During the verification process, the tag must be placed in the same position and orientation as when the EM signature was recorded in the database. Alignment is achieved with a

simple holder designed specifically for the bottle. A reference marked on the bottle can be used as an angular alignment tool.

The sensitivity to angular misalignment is investigated in Figure 18, which shows the relationship between the RMS error and the angle of misalignment.As noted in [34], the RMS error increases rapidly with increasing misalignment. Consequently, if the misalignment exceeds ± 30 degrees, the rotated tag can be effectively treated as a new tag with a rotated layout. In the mechanical rotating scanner, misalignment can be compensated by calculating the RMS error between tags by performing a circular shift of the data rows, which is equivalent to rotating the tag one angular step for each shifted row and searching for the angular position that minimizes the RMS error. The angular step around the nominal position can be reduced to improve resolution at the expense of a longer measurement time. This two-step strategy, which involves coarse alignment followed by fine alignment to determine the optimal angular offset, can mitigate misalignment problems.

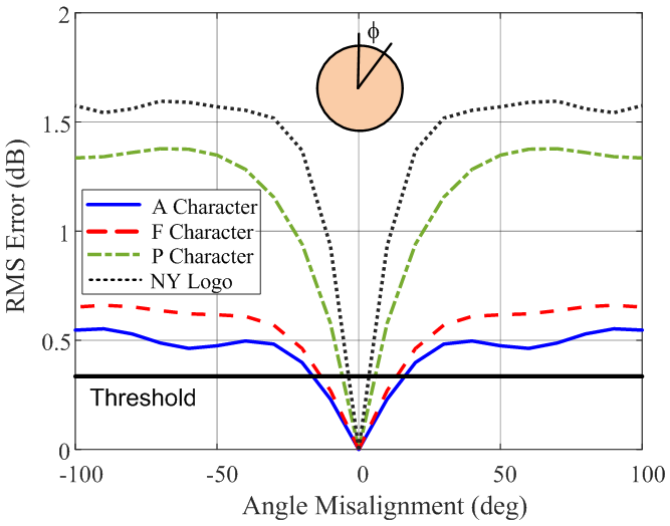

Fig. 18. Root mean square (RMS) error as a function of angular misalignment of the tags in Fig. 13 using the mechanical rotating setup.

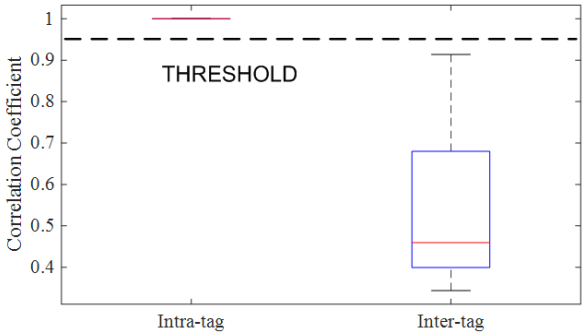

Fig. 16. Box plot of the correlation coefficient between intra-tags and inter-tags.

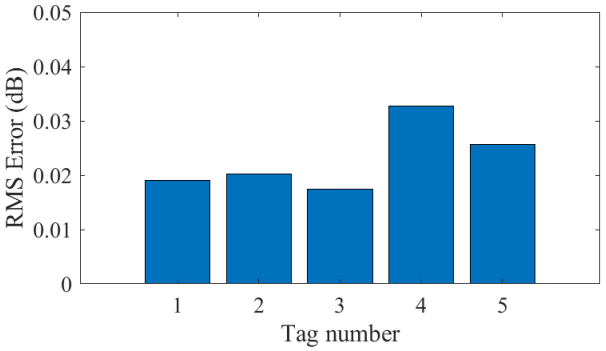

Fig. 17. Root mean square (RMS) error as a function of tag number. All tags are printed with the "F" character and manufactured with the same parameters (12% duty cycle, 24 mm/s and 900 s of electroplating time at 23 mA).

The cork is composed of cells, whose cell walls are largely made of suberin, a hydrophobic substance that naturally repels water. This is why cork is often considered water-resistant. However, cork is a porous material by nature, which allows it to absorb moisture from the environment. As moisture content increases, water molecules fill the cork's cellular structure, significantly affecting its electrical properties. In [54] it was reported that the dielectric constant increased from 1.5 to 2.7 and the loss tangent increased from 0.015 to 0.04 when comparing dry and wet cork, demonstrating the influence of humidity on its dielectric properties. These changes can introduce a small frequency shift into the electromagnetic response of the tag due to the change in effective permittivity. To evaluate the influence of moisture content, simulations have been performed on a printed "F" tag with a sheet resistance of 2.5 Ω/sq, considering different permittivities between 1.5 and 2.7, in which the cork loss tangent have also also been increased from 0.015 to 0.04 to simulate the effect of increased moisture. Fig. 19 shows that the RMS error increases up to approximately 0.12 dB, which is bellow than the typical threshold in the investigated dataset.

The scanner was placed in a climatic chamber (Memmert ICH110L, Bremen, Germany), and the relative humidity was changed between 20% and 80% according to the profile in Fig. 20.a. A stopper marked with "F" was measured over time using the switched scanner, with simultaneous humidity recordings with the network analyzer measurements. Fig. 20.b shows the difference in RMS error relative to the initial measurement. The maximum difference, attributed to variations in the dielectric constant of the materials, was approximately 0.14 dB, consistent with simulation results. The experiment revealed that the cork absorbed moisture, requiring a drying period of approximately 1 hour.

Wine bottles are usually protected with a capsule whose main function is to ensure a secure seal around the cork, preventing air from entering the bottle and potentially affecting both the quality and shelf life of the wine. The bottle capsule will minimize the impact of moisture. Wine bottle caps are typically made of various materials, each with specific purposes such as sealing, aesthetic appeal, and protection. Metal capsules, usually made of tin or aluminum, can interfere with the scanner's proper functioning and should therefore be removed before analysis. In contrast, plastic capsules, such as those made from Polyvinyl Chloride (PVC), introduce only a slight alteration in the tag's response, but they do not prevent

the measurement with the scanner, so characterization can be performed without removing PVC capsules.

Despite the protection offered by the capsule coating, an additional layer can be introduced to further protect the LIG surface and the electroplated layer of the engraved tags on wine bottle stoppers. To make counterfeiting more difficult, this additional layer, possibly made of resin or lacquer, could contain dyes that hide the tag design. Additionally, the addition of glue or other adhesives could help demonstrate product tampering, causing the tag to break when the plastic is removed. The inherently low permittivity (around 2-3) of these thin dielectric layers would mainly cause shifts in resonant frequencies, leading to a more unpredictable and distinctive tag response.

Cork is highly compressible, mainly due to its cellular structure, which consists of small, closed cells filled with air. Under moderate pressure, cork can undergo significant compression—up to 50–60% of its original volume—while maintaining excellent elastic recovery, generally returning to its original shape once pressure is released [55], [56]. Therefore, changes in the dimensions of the layout could be expected before the stopper is inserted into the bottle and after it is removed. To avoid this drawback, the characterization must be done with the stoper inserted into the bottle. In terms of thermal expansion, cork has a low coefficient of thermal expansion, providing dimensional stability over a wide temperature range. Its coefficient of linear thermal expansion is generally in the range of $40 \cdot 10^{-6} K^{-1}$ [56], which means that expansion is small with temperature changes. Therefore, to best match real-world conditions, the tag characterization with the scanner will be performed with the stopper inside the bottle and, if possible (for plastic capsules), with the protective capsule in place.

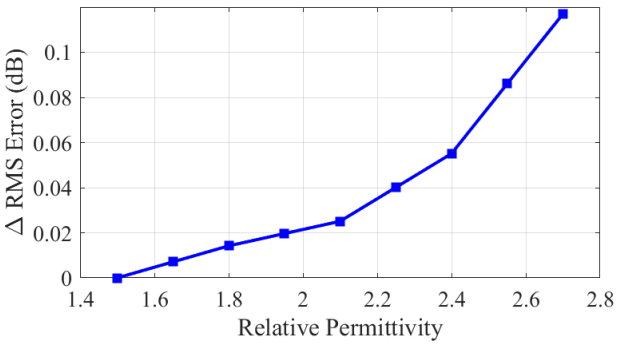

Fig. 19. Root mean square (RMS) error between tags printed with the "F" character and sheet resistance of 2.5 Ω/sq as a function of permittivity as the cork absorbed moisture. The loss tangent was linearly increased from 0.015 to 0.04.

IV. Conclusions

A method has been presented for creating unclonable tags to combat wine bottles counterfeiting. The tags are designed to have random resonance frequencies, and they have been engraved on cork stoppers using the laser-induced graphene (LIG) technique, followed by an electroplating process used

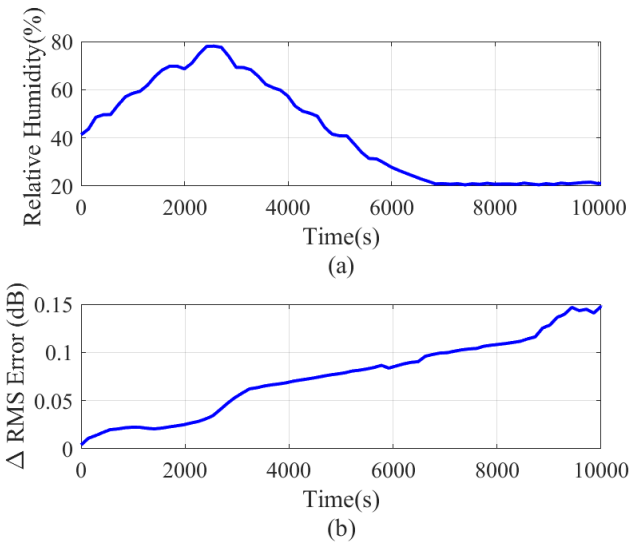

Fig. 20. (a) Measured relative humidity as a function of time. (b) Difference in the measured Root mean square (RMS) with respect to the initial measurement for a tag with character F as a function of time.

to adjust the quality factor of the resonators. Numerous manufacturing parameters enhance security by adding to natural production imperfections, making the tags difficult to be cloned. Two readers have been designed. The first reader is based on a mechanical rotating scanner. It is based on the relative rotation between a microstrip probe line and the tag with the help of a stepper motor, while the transmission coefficient is measured by a VNA in scalar mode (only magnitude information is used). In the second reader, scanning speed is improved because mechanical scanning is replaced by an electronic scanning, where four microstrip lines connected to switches and are alternatively connected to the VNA ports.

The prototype based on the rotating mechanical scanner is slower than the electronic one, even when reducing the number of angular positions, because it requires to rotate and it is more bulky. However, it allows spectrally richer electronic signatures to be obtained. The bandwidth of the electronic scanner is limited by the losses of the switch; however, there are commercially-available broadband switch models based on Monolithic Microwave Integrated Circuit (MMIC) that could be used in this application. In both types of scanners, aligning the tag with respect to a reference position marked on the cap or bottle is critical to obtain repeatable results. Taking these considerations into account, tags manufactured with the same parameters show similar classification results. Therefore, they would not require individual verification. However, statistically, tags that are more difficult to clone can be incorporated (for example, by including layout obfuscation or tamper techniques using a glue layer), which should be measured in each bottled unit, increasing the production time of these bottles.

The near-field measurement of spectral signatures in the near field enables the capture of broadband responses in a repeatable manner, avoiding the standardization issues associated with far-field chipless RFID systems. These far-field sys-

tems often encounter limitations due to regulations that restrict transmitted power and frequency allocations, which also limit their read range. Additionally, the matched transmission line probes used in this work minimize radiated emissions, thereby preventing interference with other systems. The experimental results are really promising, showing the potential of this technology for anti-fraud measures in brand protection.

REFERENCES

[1] B. Lecat, J. Brouard, and C. Chapuis, "Fraud and counterfeit wines in France: an overview and perspectives," *British Food Journal*, vol. 119, no. 1, pp. 84–104, 2017.

[2] N. C. Yiu, "An NFC-enabled anti-counterfeiting system for wine industry," *arXiv preprint arXiv:1601.06372*, 2016.

[3] W. Yao, C.-H. Chu, and Z. Li, "The use of rfid in healthcare: Benefits and barriers," in *2010 IEEE International Conference on RFID-Technology and Applications*, 2010, pp. 128–134.

[4] A. Li, J. Li, Y. Zhang, D. Han, T. Li, and Y. Zhang, "Secure uhf rfid authentication with smart devices," *IEEE Transactions on Wireless Communications*, vol. 22, no. 7, pp. 4520–4533, 2023.

[5] N. Semiconductors, "Mifare sam av3 for ntag 5, icode dna and ucode dna," accessed: April 24, 2025. [Online]. Available: https://www.nxp.com/docs/en/applicationnote/AN12698.pdf

[6] R. Pappu, B. Recht, J. Taylor, and N. Gershenfeld, "Physical one-way functions," *Science*, vol. 297, no. 5589, pp. 2026–2030, 2002.

[7] N. Soltanieh, Y. Norouzi, Y. Yang, and N. C. Karmakar, "A review of radio frequency fingerprinting techniques," *IEEE Journal of Radio Frequency Identification*, vol. 4, no. 3, pp. 222–233, 2020.

[8] E. Enakerakpo, A. Umar, M. Alhendi, R. Al-Haidari, D. J. Richmond, U. S. Somarathna, S. Gonya, M. D. Poliks, T. Rovere, M. Beckford, and J. Nichols, "Passive uhf-rfid tag with printed security features for authentication and tamper resistance," *IEEE Journal of Radio Frequency Identification*, vol. 8, pp. 49–57, 2024.

[9] V. Deepu, A. Vena, E. Perret, and S. Tedjini, "New RF identification technology for secure applications," in *2010 IEEE International Conference on RFID-Technology and Applications*, 2010, pp. 159–163.

[10] K. Yang, D. Forte, and M. M. Tehranipoor, "UCR: An unclonable chipless RFID tag," in *2016 IEEE International Symposium on Hardware Oriented Security and Trust (HOST)*. IEEE, 2016, pp. 7–12.

[11] R. de Amorim, N. Barbot, R. Siragusa, and E. Perret, "Millimeter-wave Chipless RFID Tag for Authentication Applications," in *2020 50th European Microwave Conference (EuMC)*, 2021, pp. 800–803.

[12] D. Nastasiu, R. Scripcaru, A. Digulescu, C. Ioana, R. De Amorim, N. Barbot, R. Siragusa, E. Perret, and F. Popescu, "A new method of secure authentication based on electromagnetic signatures of chipless rfid tags and machine learning approaches," *Sensors*, vol. 20, no. 21, 2020. [Online]. Available: https://www.mdpi.com/1424-8220/20/21/6385

[13] J. P. Marchand, "Microwave barcode reader using dipole antenna," apr 15 2003, uS Patent 6,547,140.

[14] E. Perret, A. Vena, S. Tedjini, Y. Boutant, and C. Halope, "Item comprising a barcode with an electromagnetic signature," jul 4 2017, uS Patent 9,697,446.

[15] M. Kheir, H. Kreft, I. Hölken, and R. Knöchel, "On the physical robustness of rf on-chip nanostructured security," *Journal of information security and applications*, vol. 19, no. 4-5, pp. 301–307, 2014.

[16] Z. A. et al., "Potential of chipless authentication based on randomness inherent in fabrication process for RF and THz," in *Proc. 11th Eur. Conf. Antennas Propag. (EUCAP)*. EuCAP, 2017, pp. 2559–2563.

[17] Z. Ali, E. Perret, N. Barbot, R. Siragusa, D. Hély, M. Bernier, and F. Garet, "Detection of natural randomness by chipless RFID approach and its application to authentication," *IEEE Transactions on Microwave Theory and Techniques*, vol. 67, no. 9, pp. 3867–3881, 2019.

[18] Z. Ali, E. Perret, N. Barbot, R. Siragusa, D. Hély, M. Bernier, and F. Garet, "Authentication using metallic inkjet-printed chipless rfid tags," *IEEE Transactions on Antennas and Propagation*, vol. 68, no. 5, pp. 4137–4142, 2020.

[19] G. DeJean, V. Lakafosis, A. Traille, H. Lee, E. Gebara, M. Tentzeris, and D. Kirovski, "RFDNA: A wireless authentication system on flexible substrates," in *2011 IEEE 61st Electronic Components and Technology Conference (ECTC)*. IEEE, 2011, pp. 1332–1337.

[20] V. L. et al., "RF fingerprinting physical objects for anticounter feiting applications," *IEEE Transactions on Microwave Theory and Techniques*, vol. 59, no. 2, pp. 504–514, 2011.

[21] S. Genovesi, S. Choudhury, A. Gharibi, F. Costa, and G. Manara, "Additive Manufacturing Technologies for Wireless Anti-Counterfeiting Solutions," in *2023 IEEE 13th International Conference on RFID Technology and Applications (RFID-TA)*. IEEE, 2023, pp. 130–133.

[22] C. Herrojo, J. Mata-Contreras, A. Nunez, F. Paredes, E. Ramon, and F. Martin, "Near-field chipless-RFID system with high data capacity for security and authentication applications," *IEEE Transactions on Microwave Theory and Techniques*, vol. 65, no. 12, pp. 5298–5308, 2017.

[23] D. Nastasiu, R. Scripcaru, A. Digulescu, C. Ioana, R. De Amorim, N. Barbot, R. Siragusa, E. Perret, and F. Popescu, "A New Method of Secure Authentication Based on Electromagnetic Signatures of Chipless RFID Tags and Machine Learning Approaches," *Sensors*, vol. 20, no. 21, 2020. [Online]. Available: https://www.mdpi.com/1424-8220/20/21/6385

[24] J. J. Fodop Sokoudjou, F. Villa-González, P. García-Cardarelli, J. Díaz, D. Valderas, and I. Ochoa, "Chipless RFID Tag Implementation and Machine-Learning Workflow for Robust Identification," *IEEE Transactions on Microwave Theory and Techniques*, vol. 71, no. 12, pp. 5147–5159, 2023.

[25] G. Khadka, B. Ray, N. C. Karmakar, and J. Choi, "Physical-Layer Detection and Security of Printed Chipless RFID Tag for Internet of Things Applications," *IEEE Internet of Things Journal*, vol. 9, no. 17, pp. 15 714–15 724, 2022.

[26] L. Huang, J. Su, Y. Song, and R. Ye, "Laser-induced graphene: En route to smart sensing," *Nano-micro letters*, vol. 12, pp. 1–17, 2020.

[27] F. Salehnia, A. Lazaro, R. Villarino, M. Lazaro, N. Canyellas, X. Vilanova, E. Llobet, and D. Girbau, "Battery-Free NFC Sub-ppm Gas Sensor for Distributed Gas Monitoring Applications at Room Temperature," *IEEE Journal of Radio Frequency Identification*, 2023.

[28] J. Liu, D. Wu, C. Liu, Q. Wang, and H. Wang, "Full-Range On-Body Strain Sensor of Laser-Induced Graphene Embedded in Thermoplastic Elastomer via Hot Pressing Transfer for Monitoring of the Physiological Signals," *Advanced Materials Technologies*, vol. 9, no. 7, p. 2301658, 2024.

[29] X. Hu, J. Wang, C. Feng, J. Yuan, Q. Wei, and H. Wang, "A comprehensive review of laser-induced-graphene for sensor applications: fabrication, properties, and performance evaluation," *J. Mater. Chem. C*, pp. –, 2025. [Online]. Available: http://dx.doi.org/10.1039/D4TC03547J

[30] F. J. Romero, A. Salinas-Castillo, A. Rivadeneyra, A. Albrecht, A. Godoy, D. P. Morales, and N. Rodriguez, "In-depth study of laser diode ablation of kapton polyimide for flexible conductive substrates," *Nanomaterials*, vol. 8, no. 7, p. 517, 2018.

[31] A. Lazaro, M. Cujilema, F. Salehnia, R. Villarino, M. Lazaro, and D. Girbau, "Laser-Induced Graphene RF Tags for Authentication Applications," *IEEE Access*, pp. 1–1, 2024.

[32] R. Ye, Y. Chyan, J. Zhang, Y. Li, X. Han, C. Kittrell, and J. M. Tour, "Laser-induced graphene formation on wood," *Advanced Materials*, vol. 29, no. 37, p. 1702211, 2017.

[33] Y. Houeix, D. Gerardo, S. Gómez-Gijón, V. Toral, N. Rodríguez, D. P. Morales, and A. Rivadeneyra, "Responsible humidity sensor by direct laser writing on cork substrate," *Advanced Sustainable Systems*, p. 2300606, 2024.

[34] A. Lazaro, M. R. Cujilema, R. Villarino, M. Lazaro, and D. Girbau, "A novel approach for wine anti-counterfeiting using laser-induced graphene chipless rfid tags on cork," *Scientific Reports*, vol. 15, no. 1, p. 12750, 2025.

[35] E. A. Ozek, S. Tanyeli, and M. K. Yapici, "Flexible graphene textile temperature sensing rfid coils based on spray printing," *IEEE Sensors Journal*, vol. 21, no. 23, pp. 26 382–26 388, 2021.

[36] A. Rivadeneyra, J. F. Salmeron, N. Rodriguez, D. P. Morales, R. Colella, F. P. Chietera, and L. Catarinucci, "Laser-fabricated antennas for rfid applications," in *2020 50th European Microwave Conference (EuMC)*, 2021, pp. 812–815.

[37] F. P. Chietera, R. Colella, A. Verma, E. Ferraris, C. E. Corcione, C. L. Moraila-Martinez, D. Gerardo, Y. H. Acid, A. Rivadeneyra, and L. Catarinucci, "Laser-induced graphene, fused filament fabrication, and aerosol jet printing for realizing conductive elements of uhf rfid antennas," *IEEE Journal of Radio Frequency Identification*, vol. 6, pp. 601–609, 2022.

[38] A. Mostaccio, G. Antonelli, R. Capuano, C. D. Natale, E. Martinelli, and G. Marrocco, "Full-lig wireless batteryless flexible sensor for the detection of triethylamine," *IEEE Journal on Flexible Electronics*, vol. 3, no. 3, pp. 90–99, 2024.

[39] Y. Houeix, F. J. Romero, D. P. Morales, N. Rodriguez, and D. Kaddour, "Novel frequency selective surface made of laser-induced graphene,"

in *2023 IEEE 13th International Conference on RFID Technology and Applications (RFID-TA)*, 2023, pp. 257–260.
[40] Y. Li, Y. Fang, Y. Huang, K. Pan, X. Xiao, X. Liu, L. Li, and Z. Hu, "Ultra-wideband, polarization-insensitive flexible metamaterial absorber base on laser printed graphene using equivalent circuit design method," *Carbon*, vol. 212, p. 118166, 2023. [Online]. Available: https://www.sciencedirect.com/science/article/pii/S0008622323004116
[41] M. A. Nyffenegger, C. Dreimol, G. Panzarasa, I. Burgert, H.-D. Lang, and H. Mathis, "Sustainable X-Band Absorber using Iron-Catalyzed Laser-Induced Graphitization on Wood," in *2022 IEEE International Symposium on Antennas and Propagation and USNC-URSI Radio Science Meeting (AP-S/URSI)*, 2022, pp. 1090–1091.
[42] A. Ferrero, F. Sanpietro, and U. Pisani, "Accurate coaxial standard verification by multiport vector network analyzer," in *1994 IEEE MTT-S International Microwave Symposium Digest (Cat. No.94CH3389-4)*, 1994, pp. 1365–1368 vol.3.
[43] D. C. Montgomery and G. C. Runger, *Applied statistics and probability for engineers*. John wiley & sons, 2010.
[44] H. Robbins, "The asymptotic distribution of the sum of a random number of random variables," *Bulletin of the American Mathematical Society*, vol. 54, no. 12, pp. 1151–1161, 1948.
[45] L. X. Duy, Z. Peng, Y. Li, J. Zhang, Y. Ji, and J. M. Tour, "Laser-induced graphene fibers," *Carbon*, vol. 126, pp. 472–479, 2018. [Online]. Available: https://www.sciencedirect.com/science/article/pii/S0008622317310370
[46] M. C. Díaz-Maroto, M. López Viñas, L. Marchante, M. E. Alañón, I. J. Díaz-Maroto, and M. S. Pérez-Coello, "Evaluation of the storage conditions and type of cork stopper on the quality of bottled white wines," *Molecules*, vol. 26, no. 1, 2021. [Online]. Available: https://www.mdpi.com/1420-3049/26/1/232
[47] J. Lin, Z. Peng, Y. Liu, F. Ruiz-Zepeda, R. Ye, E. L. Samuel, M. J. Yacaman, B. I. Yakobson, and J. M. Tour, "Laser-induced porous graphene films from commercial polymers," *Nature communications*, vol. 5, no. 1, p. 5714, 2014.
[48] P. Crook, "Corrosion of nickel and nickel-base alloys," *Corrosion: Materials*, pp. 228–251, 2005.
[49] G. Wilcox and D. Gabe, "Faraday's Laws of Electrolysis," *Transactions of the IMF*, vol. 70, no. 2, pp. 93–94, 1992. [Online]. Available: https://doi.org/10.1080/00202967.1992.11870951
[50] W.-S. Lee, H.-S. Jang, W.-S. Lee, K.-s. Oh, and J.-W. Yu, "Design of near-field chipless rfid tags and reader based on transmission line," in *2013 Asia-Pacific Microwave Conference Proceedings (APMC)*, 2013, pp. 911–913.
[51] R. Gonçalves, S. Rima, R. Magueta, P. Pinho, A. Collado, A. Georgiadis, J. Hester, N. B. Carvalho, and M. M. Tentzeris, "RFID-Based Wireless Passive Sensors Utilizing Cork Materials," *IEEE Sensors Journal*, vol. 15, no. 12, pp. 7242–7251, 2015.
[52] F. M. Nanni and G. Marrocco, "On the information content of rfid fingerprints," in *2024 IEEE International Symposium on Antennas and Propagation and INC/USNC-URSI Radio Science Meeting (AP-S/INC-USNC-URSI)*, 2024, pp. 23–24.
[53] A. Fawky, A. El-Awamry, M. Khaliel, and T. Kaiser, "Novel notch detection techniques for frequency coded chipless rfid," in *2017 IEEE 14th International Conference on Networking, Sensing and Control (ICNSC)*, 2017, pp. 345–350.
[54] R. Gonçalves, S. Rima, R. Magueta, P. Pinho, A. Collado, A. Georgiadis, J. Hester, N. B. Carvalho, and M. M. Tentzeris, "Rfid-based wireless passive sensors utilizing cork materials," *IEEE Sensors Journal*, vol. 15, no. 12, pp. 7242–7251, 2015.
[55] O. Anjos, C. Rodrigues, J. Morais, and H. Pereira, "Effect of density on the compression behaviour of cork," *Materials and Design*, vol. 53, pp. 1089–1096, 2014. [Online]. Available: https://www.sciencedirect.com/science/article/pii/S0261306913006663
[56] S. P. Silva, M. A. Sabino, E. M. Fernandes, V. M. Correlo, L. F. Boesel, and R. L. Reis, "Cork: properties, capabilities and applications," *International Materials Reviews*, vol. 50, no. 6, pp. 345–365, 2005. [Online]. Available: https://journals.sagepub.com/doi/abs/10.1179/174328005X41168

Antonio Lazaro (M'07–SM'16) was born in Lleida, Spain, in 1971. He received the M.S. and Ph.D. degrees in telecommunication engineering from the Universitat Politècnica de Catalunya (UPC), Barcelona, Spain, in 1994 and 1998, respectively. He then joined the faculty of UPC, where he currently teaches a course on microwave circuits and antennas. Since July 2004, he is a Full-Time Professor at the Department of Electronic Engineering, Universitat Rovira i Virgili (URV), Tarragona, Spain. His research interests are microwave device modeling, on-wafer noise measurements, monolithic microwave integrated circuits (MMICs), low phase noise oscillators, MEMS, RFID, UWB and microwave systems.

Marco Rodrigo Cujilema pursuing the Ph.D. degree with the Department of Electronics, Rovira i Virgili University, Spain. He held positions as a contracted Professor with Universidad Tecnológica Equinoccial (UTE), from 2019 to 2022, and a Urban Operations Technician (OPU) with Telconet, from 2023 to 2024. His research interest includes laser-induced graphene (LIG).

Marc Lazaro was born in Tarragona, Spain, in 1995. He received the BS in Industrial Electronics and Automation Engineering and the MS in Electronic Systems Engineering and Technology (METSE) from Rovira i Virgili University, Tarragona, Spain, in 2017 and 2018, respectively. Up until now, he has accumulated professional experience as a data acquisition engineer and as embedded systems developer. Since 2019 he has been working toward the Ph.D. degree in the Department of Electronics at the Rovira i Virgili University. His research activities are focused on semipassive RFID technologies based on backscattering communication and novel applications based on Millimeter wave identification (MMID).

Ramon Villarino was awarded a degree in Telecommunications Technical Engineering by Ramon Llull University (URL) in Barcelona, Spain, in 1994, a degree in Senior Telecommunications Engineering by the Universitat Politècnica de Catalunya (UPC) in Barcelona, Spain, in 2000 and a doctorate by the UPC in 2004. In 2005-2006, he was a Research Associate at the Technological Telecommunications Center of Catalonia (CTTC) in Barcelona, Spain. He worked as a Researcher and Assistant Professor at the Universitat Autònoma de Barcelona (UAB) from 2006 to 2008. Since January 2009 he has been a full-time professor at Universitat Rovira i Virgili (URV) in Tarragona, Spain. His research activities focus on radiometry, microwave devices, and systems based on UWB, RFIDs, and frequency selective structures using MetaMaterials (MM).

David Girbau (M'04–SM'13) was awarded a BSc in Telecommunication Engineering, a Master's in Electronics Engineering, and a doctorate in Telecommunication by Universitat Politècnica de Catalunya (UPC) in Barcelona, Spain, in 1998, 2002 and 2006, respectively. From February 2001 to September 2007 he was a Research Assistant at UPC. From September 2005 to September 2007 he was a part-time Assistant Professor at Universitat Autònoma de Barcelona (UAB). Since October 2007 he has been a full-time professor at Universitat Rovira i Virgili (URV) in Tarragona, Spain. His research interests include microwave devices and systems, with an emphasis on UWB, RFIDs, RF-MEMS and wireless sensors.